Fully automated segmentation of oncological PET volumes using a combined multiscale and statistical model

David W. G. Montgomery
School of Electronics, Electrical Engineering and Computer Science, ECIT, The Queen's University of Belfast, Belfast, Northern Ireland

Abbes Amira
School of Engineering and Design, Brunel University, London, Uxbridge, United Kingdom

Habib Zaidi[a)]
Division of Nuclear Medicine, Geneva University Hospital, CH-1211 Geneva 4, Switzerland

(Received 7 June 2006; revised 20 December 2006; accepted for publication 20 December 2006; published 29 January 2007)

The widespread application of positron emission tomography (PET) in clinical oncology has driven this imaging technology into a number of new research and clinical arenas. Increasing numbers of patient scans have led to an urgent need for efficient data handling and the development of new image analysis techniques to aid clinicians in the diagnosis of disease and planning of treatment. Automatic quantitative assessment of metabolic PET data is attractive and will certainly revolutionize the practice of functional imaging since it can lower variability across institutions and may enhance the consistency of image interpretation independent of reader experience. In this paper, a novel automated system for the segmentation of oncological PET data aiming at providing an accurate quantitative analysis tool is proposed. The initial step involves expectation maximization (EM)-based mixture modeling using a *k*-means clustering procedure, which varies voxel order for initialization. A multiscale Markov model is then used to refine this segmentation by modeling spatial correlations between neighboring image voxels. An experimental study using an anthropomorphic thorax phantom was conducted for quantitative evaluation of the performance of the proposed segmentation algorithm. The comparison of actual tumor volumes to the volumes calculated using different segmentation methodologies including standard *k*-means, spatial domain Markov Random Field Model (MRFM), and the new multiscale MRFM proposed in this paper showed that the latter dramatically reduces the relative error to less than 8% for small lesions (7 mm radii) and less than 3.5% for larger lesions (9 mm radii). The analysis of the resulting segmentations of clinical oncologic PET data seems to confirm that this methodology shows promise and can successfully segment patient lesions. For problematic images, this technique enables the identification of tumors situated very close to nearby high normal physiologic uptake. The use of this technique to estimate tumor volumes for assessment of response to therapy and to delineate treatment volumes for the purpose of combined PET/CT-based radiation therapy treatment planning is also discussed. [DOI: 10.1118/1.2432404]

Key words: positron emission tomography, medical image segmentation, multiscale Markov modeling, Gaussian mixture modeling, wavelet

I. INTRODUCTION

Diagnosis, staging, treatment, prognosis, and follow-up are the main components in the management of cancer, and positron emission tomography (PET) plays a central role in all these components. Due to its high sensitivity and ability to model function, it is effective in targeting specific functional or metabolic signatures that may be associated with various types of disease. Among all diagnostic and therapeutic procedures, PET is unique in the sense that it is based on molecular and pathophysiological mechanisms and employs radioactively labeled biological molecules as tracers to study the pathophysiology of the tumor *in vivo* to direct treatment and assess response to therapy.[1] The leading current area of clinical use of PET is in oncology, where ^{18}F-FluoroDeoxyGlucose (FDG) remains the most widely used tracer. FDG-PET has already had a large valuable effect on cancer staging and treatment and its use in clinical oncology practice continues to evolve.

Current procedures for interpreting oncological clinical data in many PET facilities are still based on mere visual assessment, thereby increasing observer variance. It is deplorable that clinical practice continue to evolve in this direction if we are to give meaningful information to the referring clinicians. Quantification tools supporting the visual interpretation of the PET physician with meaningful data and a format to display the results are thus highly desired. Manual approaches for semi-quantitative assessment of lesions' uptake using the widely used standardized uptake value (SUV) index have shown their limitations.[2] Automatic quantitative assessment of metabolic PET data is attractive

and will certainly revolutionize the practice of functional imaging since it can lower variability across institutions and may enhance the consistency of image interpretation independent of reader experience. To achieve this goal image segmentation, which is the process of classifying the voxels in an image into a set of distinct classes, allows to extract specific features (e.g., lesions) from the PET image.

Within the realm of diagnostic PET imaging, image segmentation is vital for a variety of specific applications, namely, to correct attenuation effects in PET and to alleviate artifacts introduced through image reconstruction using tissue component density association,[3,4] or tumor quantification in staging, a process that analyses the development of tumors over time,[5] and to aid in radiation therapy treatment planning.[6–9]

Plenty of image segmentation approaches were proposed including thresholding, region growing, classifiers, clustering, edge detection, Markov random field models, artificial neural networks, deformable models, and atlas-guided and many other approaches.[10] Scalar images can be segmented using thresholding approaches by partitioning image intensities. Multithresholding occurs when more than one threshold value is determined.[11] When images contain different structures with contrasting intensities, thresholding provides a simple but effective means for obtaining segmentation. Generally, the thresholds are generated based on visual assessment of the resulting segmentation, however, automated methods do exist.[11–13]

The majority of the work performed on PET image segmentation utilizes thresholding.[14] An investigation into the effect of threshold size on the segmentation and quantification of simulated tumors in PET for the staging and radiotherapy treatment planning of non-small-cell lung cancer has been reported.[15] Results show that higher image thresholds are required to accurately render the smallest simulated tumors. Similar work was performed elsewhere.[14,16–18] The main limitation of thresholding is that the results are coupled too tightly with the thresholds used, where any change can completely alter the result of the segmentation. Furthermore, thresholding does not consider the spatial characteristics of an image, thus causing it to be sensitive to noise and intensity fluctuations. For this reason, it cannot be easily applied to many medical imaging modalities. These drawbacks essentially corrupt the histogram of the image, making partitioning via the selection of appropriate thresholds more problematic. Data clustering is another effective technique for image segmentation. The advantage of clustering is that it can be applied to a multi-band image such as a color image or image composed of multiple feature layers.[5]

An alternative is to use a Markov random field model (MRFM), which is a statistical approach that can be utilized within segmentation methodologies to model spatial interactions between nearby pixels. These local correlations between pixels are used as a mechanism for modeling various image properties. From a medical imaging perspective, this kind of analysis is useful as most pixels can be categorized into the same class as their neighbors. Although possible, it is unlikely that any anatomical structure consists of only one pixel under MRFM assumptions.[19] As a MRFM is not specifically a segmentation method, it is often incorporated into other segmentation systems such as the *k*-means or fuzzy c-means algorithms under a Bayesian prior model.[20] Given the image data, the segmentation is achieved by maximizing the *a posteriori* probability of the segmentation, obtained using iterative methods such as iterated conditional modes or simulated annealing.[21]

Recent work utilizing this statistical methodology for medical image segmentation includes a comprehensive system developed to overcome the problem of partial volume voxels that contain a mixture of two or more tissue types.[22] An automated segmentation procedure for neurological MRI was also developed to overcome some of the problems associated with multidimensional clustering techniques such as partial volume effect and the difficulty of incorporating *a priori* knowledge.[23] Problems associated with a MRFM include the accurate selection of the parameters controlling the strength of spatial interactions. Incorrect selection of this parameter may result in a loss of important structural detail and an excessively smooth segmentation. In the medical imaging context, the loss of anatomical detail is possible and areas of diagnostic significance may be incorrectly represented. Furthermore, these approaches typically require computationally intensive algorithms. Resulting segmentations obtained using this methodology are robust to noise and do not exhibit many small disconnected regions that are apparent using non-Markovian approaches.

In this paper, a novel unsupervised spatial segmentation methodology and performance evaluation of the approach is presented. This system, developed for volumetric PET analysis, is based on multiscale principles, whereby a series of image wavelet scales is used in conjunction with a MRFM to segment data based on the relationship of a voxel with its neighbors. Wavelet methodology is employed to aid in the analysis of image structures not apparent through modeling in the spatial domain. An overview of the complete segmentation system is provided and followed by the presentation of marginal segmentation utilizing a novel algorithm known as the minimum distance *k*-means expectation maximization (MDKEM) and a description of a general spatial domain Markov model. The multiscale modeling strategy describing how an image is decomposed into a series of redundant wavelet scales, how useful scales are selected, and how these multiple scales are processed simultaneously within a Markov modeling framework to obtain a wavelet domain segmentation is introduced. Some three-dimensional (3-D) segmentation results of an anthropomorphic thorax phantom and whole-body oncologic PET data, deemed to be problematic, are also illustrated and discussed.

II. MATERIALS AND METHODS

A. Overview of image segmentation system

The complete, automated, unsupervised PET image segmentation system is summarized in the following points:

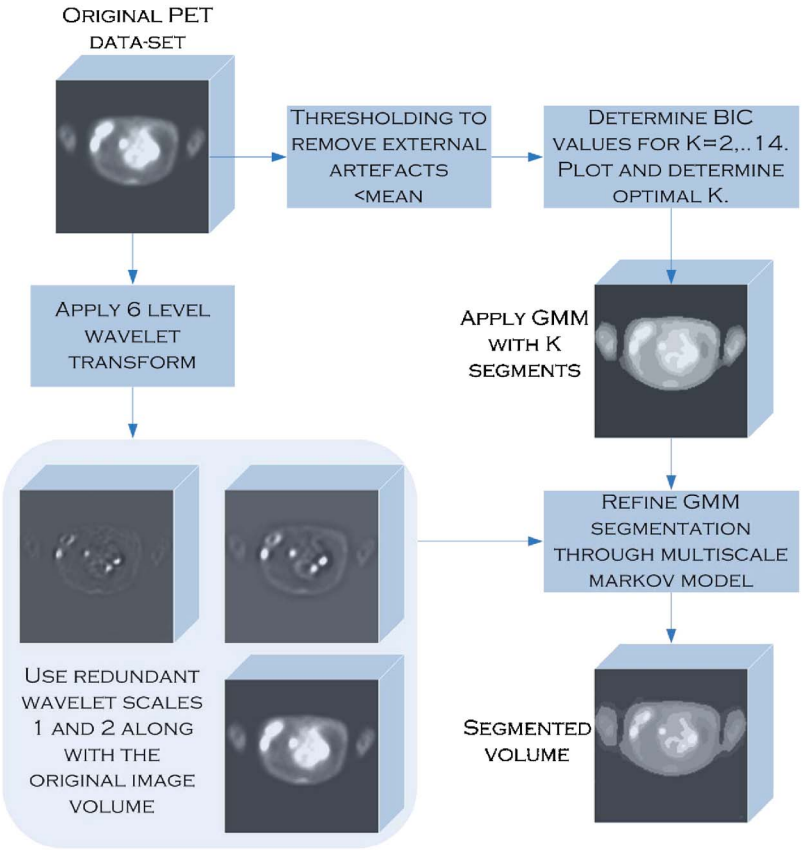

FIG. 1. Flowchart of the automated PET image segmentation system.

(1) Thresholding is performed to remove artifacts external to the object to be segmented. The data mean is calculated and voxels with intensity less than this mean are set to zero. This type of procedure is suitable for this application due to the distribution of intensity values through images of this nature. As the total volumetric image comprises predominantly of background, the mean of the data is typically low, and, therefore, this preprocessing step can alleviate artifacts within the image background, without jeopardizing imperative data features.

(2) An initial segmentation of the 3-D image is performed in the spatial domain. This process is based solely on voxel intensities and uses a specified number of clusters. This is initiated using a new *k*-means clustering variant that modifies sample order to find a solution with the lowest average Euclidean distance. We recall that the *k*-means clustering algorithm clusters data by iteratively computing a mean intensity for each class and segmenting the image by classifying each pixel in the class with the closest mean. The popular expectation maximization (EM) algorithm, which unifies various previous statistical approaches.[24] is then applied to fit a Gaussian mixture model and to locate a marginal segmentation through maximum likelihood (ML) classification.

(3) The marginal segmentation achieved in step 2 is refined using a novel multiscale MRFM to segment the data based on the relationship of a voxel with its neighbors:

- The original 3-D image volume is decomposed using the *à trous* wavelet transform.
- Six wavelet scales are specified and the first two are utilized.
- The original image and selected wavelet scales are used in conjunction with a MRFM, with all selected images being considered through the utilization of multivariate Gaussian density calculations.

The entire image segmentation system flowchart is illustrated in Fig. 1. The optimal number of clusters is determined by the Bayes information criterion (BIC), which is a one-hypothesis testing methodology that uses Bayesian inference[25] The BIC is employed to approximate the Bayes factor, which is consequently used to compare a series of rival theories. Over the last decade, the BIC has gained notoriety as a significant methodology for model selection. This model does not consider the complete parameter set obtained from the multiscale MRFM. The set of parameters attained via marginal segmentation of the original image, where the conditional likelihoods are considered to be Gaussian, are exploited as an alternative. Although the BIC does not allow for spatial correlations between voxels to be considered, it does provide a useful strategy for the comparison of contesting models. Marginal segmentation is performed using the MDKEM algorithm.

B. Minimum distance *k*-means EM (MDKEM)

To compute the optimal marginal segmentation, an initial range of intensity values associated with each cluster is allo-

cated, from which the EM algorithm.[24,26] can determine optimal intensity ranges. The selection of these initialization parameters is complex and greatly influences the overall segmentation result. This relates to the fundamental limitation associated with the EM algorithm. The algorithm is not guaranteed to converge to a global maximum of the likelihood, and, rather, is susceptible to local maximum convergence[27] In real world applications, little focus is placed on determining good initialization parameters, with random estimates and equal intensity partitioning as the favored approaches due to their simplicity. In Ref. 28, the *k*-means algorithm is used to initialize EM in a motion tracking application, however, only a simplistic implementation is employed.

In addition to initialization, different clustering solutions are obtained depending on the order of image samples. By utilizing *k*-means, cluster means are recomputed after each change in cluster membership. From these migrating means, it is evident that the final cluster solution is to some extent dependent on the order in which the cases are considered for relocation. Case order dependence led to the development of the novel marginal segmentation system known as the MDKEM. This marginal system is inspired from the work of Wishart, who developed the so-called "Focal Point" procedure.[29] This randomizes the case order of the data being utilized, so that different cluster solutions are obtained from different *k*-means runs. Focal Point stores information on the different solutions obtained and reports those solutions with the smallest Euclidean sum of squares. MDKEM is described as follows:

(1) *k*-means is initialized by means based thresholding where the thresholds were randomly selected.
(2) Voxel intensities are resampled into a 1-D signal.
(3) The sample or case order is randomized so different cluster solutions are obtained from different *k*-means runs.
(4) *n* randomization procedures are applied and details on each solution are stored.
(5) The solution that results in the smallest average Euclidean distance measurement is considered the most satisfactory and this solution is used for EM initialization.

Basically, the popular *k*-means clustering algorithm assumes that the data form distinct spheres around *k* centers. The number of randomization procedures *n* used in the fourth step of the MDKEM algorithm was determined experimentally over a large number of data sets and the optimal value yielding the best segmentation results for a reasonable computing time was found to be close to 10.

C. Spatial modeling using a traditional Markov random field model

To model an image using a MRFM, starting parameters are determined. Parameters required to model the spatial characteristics of an image are obtained using the marginal segmentation detailed in the previous section. The result of marginal segmentation is considered to be a baseline scene estimate and a spatial model is used to refine the segmentation obtained.

1. The Potts/Ising model

Spatial dependence within an image can be modeled using a Markov random field to characterize each voxel's true state.[30–32] An assumption is made that a true hidden state X_i exists for each voxel i where X_i is an integer representation of one of the K states ($X_i \in \{1,2,\ldots,K\}$) and that a voxel's true state is likely to be similar to the states associated with its neighboring voxels. An indicator function is defined $I(X_i,X_j)$ that equates to 1 when $X_i=X_j$ and 0 in all other cases. $N(X_i)$ represents the voxels neighboring voxel X_i (the neighborhood size is discussed in a later subsection) and $U(N(X_i),k)$ signifies the number of voxels in $N(X_i)$ with state k. As the Markov random field is used to define spatial structure on X, the *Potts or Ising* model is described mathematically in the following equation, where the sum is computed over all neighbor pairs:

$$p(X) \propto \exp\left(\phi \sum_{i,j} I(X_i,X_j)\right). \tag{1}$$

The amount of spatial homogeneity within the model is expressed using the parameter ϕ, a value that implies either randomness or uniformity. Where ϕ is positive, neighboring voxels are similar; however, when the value associated with this parameter is negative, it indicates that neighboring voxels are dissimilar. Dissimilarity between neighboring voxels is not of interest in this study. From $p(X)$ characterized in Eq. (1), the following conditional distribution can be derived:

$$p(X=j|N(X_i),\phi) = \frac{\exp\left[\phi U(N(X_i),j)\right]}{\sum_k \exp\left[\phi U(N(X_i),k)\right]}. \tag{2}$$

This model is referred to as a hidden MRFM as the variables X can only be determined through the set of all observed image voxels Y. In this study, boundary voxels, voxels that exist on the image boundary, are excluded from analysis, except in their use as outlying neighbors of interior voxels not situated on the image boundary. These voxels are not considered, as their full set of neighbors cannot be observed.

2. The iterated conditional modes (ICM) algorithm

The defined spatial segmentation is based on the ICM algorithm introduced by Besag.[32,33] This algorithm is used for image reconstruction when local true image characteristics are modeled under Markovian principles. Specifically, this approach can be used collaboratively with the Potts/Ising model described previously. [See Eq. (1).] This iterative algorithm commences using an initial estimate of the true scene X, referred to as $\hat{X}$, and proceeds to compute estimates for the parameters associated with $p(Y_i|X_i)$ in addition to ϕ and X. Considering the X values are latent and the original image voxels Y_i can be observed, an assumption is made that the conditional density model, linking the observed and la-

tent spaces $f(Y_i|X_i=j)$, follows a Gaussian distribution with mean m_j and variance σ_j^2. From this assumption, it is apparent that the Y values are conditionally independent as a result of the X values [shown in Eqs. (3) and (4)]. θ_k represents the set of parameters(μ,σ^2) for the state K.[30]

$$f(Y|X)=\prod_i f(Y_i|X_i), \tag{3}$$

$$f(Y_i|X_i)=f(Y_i|\theta_{X_i}). \tag{4}$$

The ICM algorithm is initialized using marginal segmentation by Gaussian mixture modeling to find $\hat{X}$, the preliminary scene estimate. The algorithm proceeds as follows:[30,33,34]

(1) The Gaussian parameters $\hat{\theta}$ are updated by maximizing the likelihood in Eq. (3) using the most current update of $\hat{X}$. Mathematically, maximum likelihood estimates of μ_j and σ_j^2 for each class j are determined, using $\hat{X}$ as the voxel assignment to a given cluster to update $\hat{\theta}=\arg\max f(Y|\hat{X})$.

(2) Utilizing the current estimate $\hat{X}$ as the true scene, ϕ is estimated using maximum pseudolikelihood [shown in Eqs. (5) and (6)]. The function to be maximized is the product over all voxels from Eq. (2):

$$PL(\hat{X}|\phi)=\prod_i p(\hat{X}_i|N(\hat{X}_i),\phi), \tag{5}$$

$$\hat{\phi}=\arg\max_{\phi} PL(\hat{X}|\phi). \tag{6}$$

By maximizing the function for all image voxels, one ϕ parameter exists for the complete image, which dictates that the same amount of spatial cohesion exists within each segment. The estimation of ϕ is used to investigate whether segments have been correctly estimated. Specifically, this value locates segments that have been incorrectly combined, indicating high spatial cohesion, or incorrectly subdivided, indicating low cohesion. When the number of true natural groupings K_T is greater than or equal to the number of assumed groupings K, the ϕ parameter is correctly estimated; however, as K grows beyond K_T, an underestimated value of ϕ is expected. In cases where this occurs, the ϕ estimate can be negative, even when the ϕ associated with the true scene is positive, and, for this reason, ϕ is constrained to be positive by resetting to zero if required, before continuing.

(3) Update $\hat{X}$ by individually considering each voxel and replacing $\hat{X}_i$ with the state that maximizes the following equation:

$$\hat{X}_i=\arg\max_j f(Y_i|X_i=j)p(X_i=j|N(\hat{X}_i),\hat{\phi}). \tag{7}$$

On the completion of the voxel updating procedure, a new $\hat{X}$ is obtained. After one iteration of ICM, updated estimates of $\hat{\theta}$, $\hat{\phi}$, and $\hat{X}$ are determined. ICM concludes either on convergence of $\hat{X}$ or when a predetermined number of iterations has been reached. In this instance, the maximum number of iterations is set to 20; however, in other studies only ten iterations were utilized.[30]

When working within a MRFM, an exact neighborhood definition is required. From a purely two-dimensional perspective, a pixel neighborhood is straightforward to define and is typically the eight pixels surrounding the pixel in question.[30] The definition of neighborhood size, when utilizing a 3-D MRFM for volumetric image analysis, is considerably more complex. Numerous neighborhood possibilities exist; however, in this study one of the more standard approaches is used. The selection of an appropriate neighborhood is of utmost importance and essentially controls the level of segmentation smoothness. Too large a neighborhood results in an overly smooth segmentation conveying little or no shape information, and, alternatively, an inappropriately small neighborhood can cause certain cluster volumes to be underestimated. It is vital to find a compromise as, particularly within medical applications, segmentation accuracy is imperative.

For 3-D modeling, a neighborhood is defined as the 26 voxels surrounding a specific voxel. Eight of these neighbors are located around this voxel in the same axial plane, while the remaining 18 neighbors are situated in the prior and subsequent image frames. This neighborhood is employed to regulate how readily the Markov model can refine the initial segmentation, and, in the multiscale case, substantial clustering modifications are required. This neighborhood is chosen as it considers all direct neighbors, without resulting in an overly smooth segmentation. Computation time is the fundamental limitation of this neighborhood. Other neighborhoods such as the "fence," which considers 18 direct neighbors, can be easily incorporated into the system.

D. Multiscale modeling

A novel multiscale extension to the traditional MRFM is described in the following subsections. This extension is introduced, as multiresolution approaches yield a series of scale components, allowing for the evaluation of spatial relationships between objects at multiple scales. Image characteristics associated with a particular scale, which may go undetected using other analysis techniques, can therefore be exploited.[35] An overview of the proposed 3-D multiscale Markov model is given below:

(1) Obtain an initial segmentation through marginal segmentation using the MDKEM algorithm discussed in Sec. II B.
(2) Perform an *à trous* wavelet decomposition on the original image volume to obtain a set of scale components.
(3) Determine scales deemed significant for image analysis.
(4) Utilize the original image volume and significant wavelet scales within a MRFM to refine the original marginal segmentation.

In Sec. II D 1, the mathematical theory encompassing the *à trous* redundant wavelet transform.[36] is presented. The scale selection criterion used to determine significant wavelet

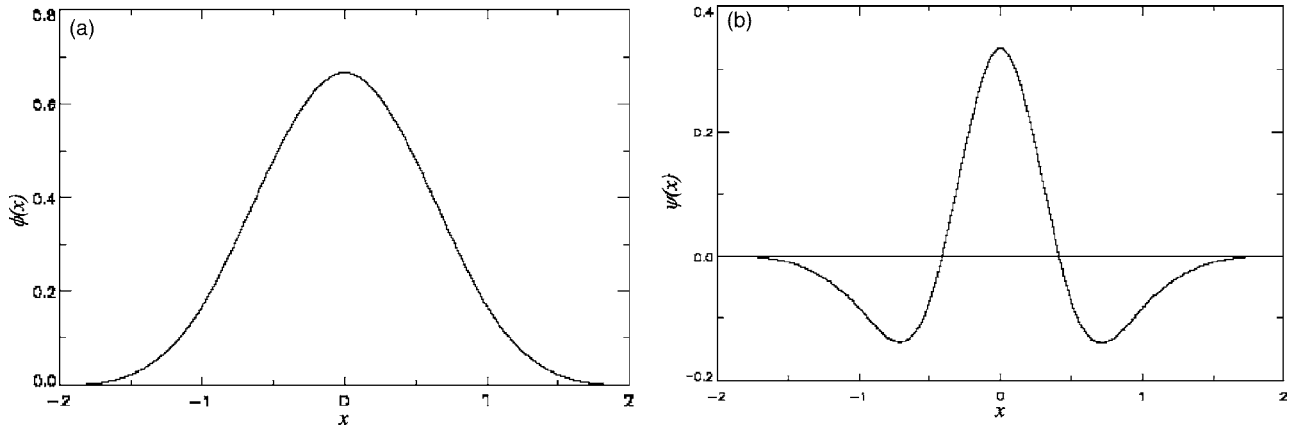

FIG. 2. Plots of the (a) scaling function and (b) wavelet function.

scales is described in Sec. II D 2. Section II D 3 highlights how this series of scales is utilized within a Markov model for segmentation refinement.

1. The à trous redundant wavelet transform

A wavelet transform decomposes a signal into a set of resolution related views. The wavelet decomposition of an image creates at each scale j, a set of coefficient values w_j with an overall mean of zero. Using the *à trous* wavelet transform, this set of coefficient values w_j contains the same number of voxels as the original 3-D image volume and, therefore, this wavelet transform is redundant. A nondecimated or redundant wavelet transform is useful for the detection of fine features within the signal. These may not be apparent using decimated transforms due to the inclusion of aliasing biases.[37]

The wavelet function is defined as the difference between the scaling functions of two successive scales. This is described mathematically as follows:

$$\frac{1}{2}\Psi\left(\frac{x}{2}\right) = \phi(x) - \frac{1}{2}\phi\left(\frac{x}{2}\right). \tag{8}$$

In this study, the third degree B-spline is used as the scaling function $\phi(x)$ with filter coefficients:

$$h = \left\{\frac{1}{16}, \frac{1}{4}, \frac{3}{8}, \frac{1}{4}, \frac{1}{16}\right\}. \tag{9}$$

This scaling function is selected due to its useful interpolation properties. The associated wavelet function ψ resembles a Mexican hat function with a central peak and negative side lobes. These functions are shown graphically in Fig. 2. The following simple algorithm has been derived to compute the associated wavelet transform:[36,37]

(1) Initialize j to zero and commence with the data $c_j(k)$ where k refers to the sample position.
(2) Increment j and perform a discrete convolution of the data $c_{j-1}(k)$ using the filter h. This can be described mathematically by

$$c_j(k) = \sum_l h(l)c_{j-1}(k + 2^{j-1}l). \tag{10}$$

The distance between the central voxel and the exterior adjacent voxels is 2^{j-1} and is related to the name given to this transform, "with holes."[36]
(3) On the completion of the previous smoothing step, the discrete wavelet transform is obtained by

$$w_j(k) = c_{j-1}(k) - c_j(k). \tag{11}$$

(4) If $j < p$, where p is the number of resolutions required, return to step 2.
(5) The wavelet transform of the data is represented by the set

$$W = \{w_1, \ldots, w_p, c_p\}. \tag{12}$$

A series expansion of the original image c_0, in relation to its wavelet scale levels, is as follows:

$$c_0(k) = c_p + \sum_{j=1}^{p} w_j(k). \tag{13}$$

This equation provides a method by which to reconstruct the original signal and, essentially, is obtained by an addition of the smoothed array $c_p(x)$ to the differences w_j.

The characteristics associated with a particular wavelet transform, and specifically, the *à trous* redundant wavelet transform, are thoroughly discussed in Refs. 36 and 37. For a fixed number of scales, the computational complexity of this algorithm is $O(n)$ for an input of length n and is therefore less complex than the fast Fourier transform (FFT).

Boundary treatment. Due to the nature of the interspersed convolution used within the *à trous* framework, careful attention is required in the treatment of signal boundaries. Although numerous strategies exist, an approach is utilized that is simple but extends the signal using coefficients that only minimally alter the statistical characteristics of the signal. This approach, known as "periodic symmetry,"[38] illustrated in Fig. 3, provides a more logical solution than overly simplified approaches that extend the signal boundaries using zero coefficients. In Fig. 4, a four-level redundant wavelet

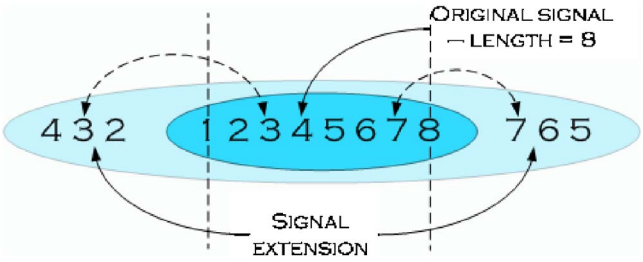

FIG. 3. 1-D signal extension using "periodic symmetry."

decomposition of a PET image slice is illustrated, while in Fig. 5, a numerical 1-D decomposition is given.

The 3-D à trous wavelet decomposition. The extension of the 1-D *à trous* wavelet decomposition into three dimensions is not trivial. The implementation used in this paper is based on one 3-D nonseparable convolution and can be described as follows:

(1) A simple function is used to translate the 1-D spline filter coefficients into a direct set of 3-D filter coefficients.
(2) The 3-D image volume is extended using periodic symmetry in all three dimensions. The extension length remains dependent on the step size, a value dictated by the level of decomposition.
(3) A nonseparable direct 3-D convolution is performed between the 3-D spline filter matrix and the image volume. The nature of this interspersed 3-D convolution results in an implementation more problematic than traditional convolution methodologies.
(4) The remainder of the 3-D decomposition follows directly from the 1-D *à trous* wavelet decomposition, described above.

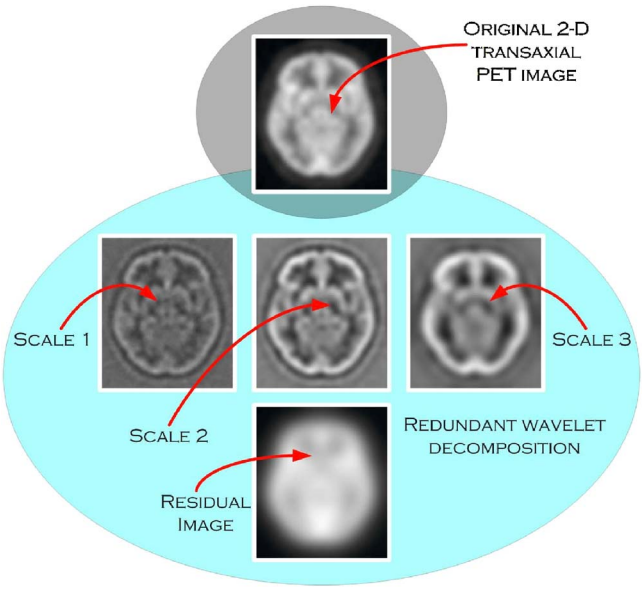

FIG. 4. Illustration of four level redundant wavelet decomposition of 2-D transaxial PET slice of human brain.

The application of the *à trous* redundant wavelet transform to a 3-D image volume results in a 4-D decomposition consisting of a specified number of 3-D wavelet scales, with dimensions equating to the original image.

2. Scale selection criterion

In this study, a wavelet transform is utilized, which decomposes 3-D data sets into six wavelet scales. In earlier work,[39] no objective selection mechanism is identified. Mid-level wavelet scales are used, with the highest and lowest wavelet scales having been rejected. The first scale is ignored under the assumption that the majority of image noise is localized within the scale; however, this is performed on several imaging modalities.[40] The residual wavelet scale is ignored as it contains averaging coefficients with high numerical values, which, if processed, can lead to an overly smooth segmentation.

Subsequent testing reveals that the rejection of the residual scale is warranted; however, the initial assumption regarding the elimination of the first wavelet scale is questionable. Although this scale undoubtedly contains the highest frequency information, this, in the PET instance, does not necessarily refer to noise, due to the use of sophisticated normalized attenuation weighted, ordered subset, expectation maximization (NAW-OSEM) iterative reconstruction algorithm[41] used to reconstruct the PET data. This reconstruction algorithm incorporates automated noise modeling. The first wavelet scale does not, therefore, need to be eliminated, as the spatial Markov model is sufficiently robust to deal with such high noise levels. The finest image features are contained within this scale, features that are vital for the production of high quality segmentation. The second wavelet scale is also utilized due to the high amount of detail that it provides.

Only two scales are selected for inclusion within the multiscale MRFM, as after marginal segmentation, baseline segmentation is achieved. These scales are included to reveal more information on finer image features and to model the data from a spatial perspective. The reason for selecting only scales one and two in redundant wavelet is that these two scales contain the necessary information in the processed images with higher entropy value, which gives better segmentation. An entropy analysis is used for the selection of the wavelet scales. In addition, as computation time within the Markov model is related to the number of scales under consideration, the use of these scales prevents computation time from becoming excessive.

3. Processing multiple scales within the MRFM

To implement a multiscale MRFM, a mechanism must be contrived to amalgamate the salient information from each à trous wavelet scale. To achieve this, the traditional MRFM must be modified. These modifications are outlined in the following points:

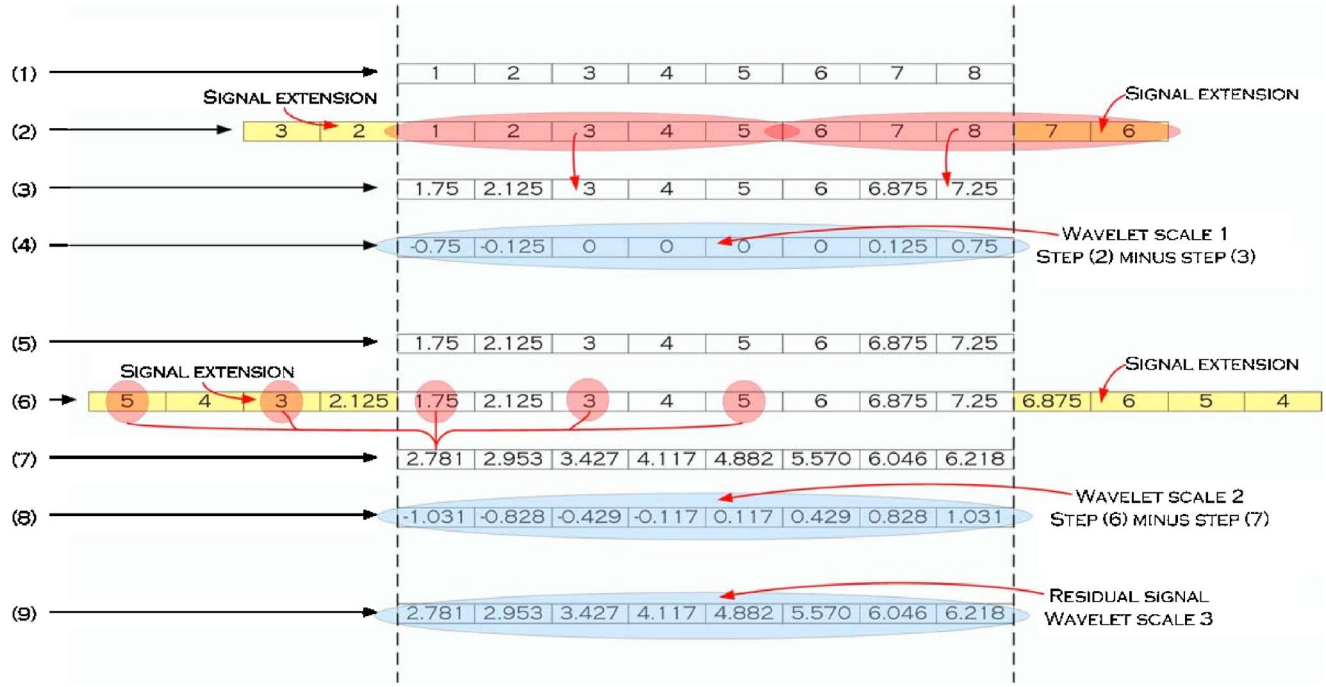

FIG. 5. Three-level *à trous* wavelet decomposition of 1-D signal.

(1) In conjunction with the original image, the first two redundant wavelet scales are considered. The original image volume must be included within the model to stabilize the segmentation. Without its inclusion, a deterioration in segmentation quality may be evident.
(2) In the traditional MRFM, statistics associated with the initial marginal clustering solution are determined. Specifically, the mean and variance of each cluster is computed. In this multiscale system, a more thorough set of statistics is required for a later computation, which will essentially analyze the varying statistical characteristics between scales. In this multiscale system, means and covariances are determined through association with the initial marginal segmentation solution. In addition, the determinant of the variance/covariance matrix associated with each cluster is obtained. The covariance of a series of variates provides a measure of correlation strength.
(3) Step 2 of the ICM algorithm requires no modification for multiscale compliance as the estimation of ϕ is obtained using the most recent clustering estimate.
(4) To incorporate vital information from each scale, ICM step 3 must be altered. In spatial domain Markov modeling, a univariate Gaussian density is calculated for each voxel; however, in this multiscale approach, a multivariate Gaussian density must be computed where the variates refer to the intensity values associated with a particular voxel location in each selected wavelet scale. This multivariate density function for a given cluster is as follows:

$$\Phi\{w_1,\ldots,w_N\}=\frac{1}{(2\pi)^{N/2}|\sum|^{1/2}}\left\{-\frac{1}{2}\left[\sum_{q=1}^{N}\left(\sum_{p=1}^{N}(w_p-\mu_p)\times\sum_{qp}^{-1}(w_q-\mu_q)\right)\right]\right\}, \tag{14}$$

where w refers to the voxel intensities across image scales (shown in Fig. 6), and N is the number of images/scales utilized. Σ is an $N\times N$ covariance matrix for a specified cluster and $|\Sigma|$ is the determinant of Σ.

This multivariate density is used with ϕ to compute the

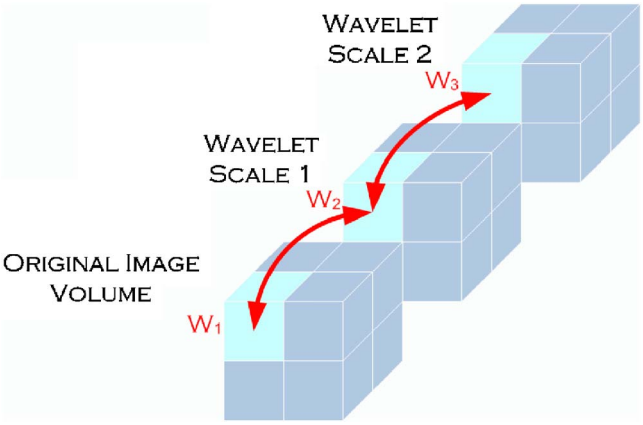

FIG. 6. Definition of w, required for multivariate density calculation.

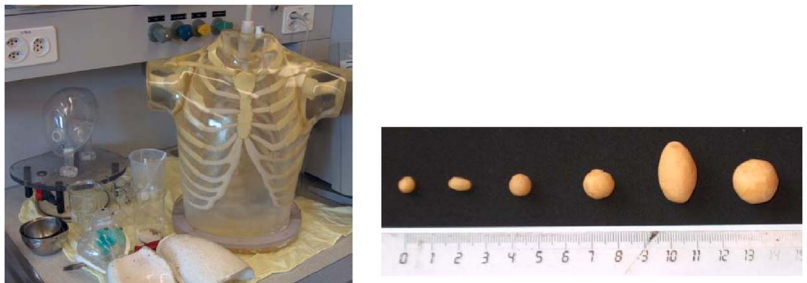

(a) (b)

FIG. 7. Photographs of the anthropomorphic thorax phantom (a) and wall-less small radioactive lesions using moulted wax tumors inserted in the left and right lungs of the phantom to simulate typical lesions in lung cancer patients.

updated current cluster probabilities and therefore readjust the clustering solution achieved on the previous ICM iteration or by marginal segmentation.

E. PET data acquisition and reconstruction

The ECAT ART (CTI/Siemens, Knoxville, TN) rotating whole body 3-D tomograph, upgraded to use collimated point sources of ^{137}Cs and capable of producing high quality scatter-free data in this continuously rotating partial-ring tomograph, was used. This allows increasing the count statistics while drastically diminishing the acquisition time.

To assess the performance of the developed segmentation algorithm, experimental measurements of the anthropomorphic thorax phantom (Radiology Support Devices Inc., Long Beach, CA) were performed [Fig. 7(a)]. This phantom consists of lungs, cardiac insert, and a liver compartment that can be filled independently. In addition, there is a plastic vial placed in the pelvis to simulate the bladder and thus take into account out of field-of-view activity. Activity concentration in the lesions was measured to be 40 times that of the lungs, which in turn was two times less than that of soft-tissue background. Lung density averaged 0.30 g/cm^3.

We have constructed a set of ellipsoidal tumors of different size using a technique proposed by Turkington *et al.*[42] that can be used to produce wall-less small radioactive lesions using molted wax [Fig. 7(b)]. These lesions mixed with ^{18}F activity having volumes ranging between 1.4 and 3.1 ml were embedded in the upper and lower parts of the left and right lungs within the physical anthropomorphic thorax phantom. This arrangement provides properties similar to the human thorax suitable for mimicking whole-body oncological FDG-PET studies.

The PET image segmentation algorithm was tested on ten oncological patients referred to the division of nuclear medicine of Geneva University Hospital for clinical evaluation of the segmentation system. All patients had plasma glucose checked before intravenous injection of 222 MBq of [^{18}F]-FDG adjusted to 70 kg body weight (none of them was diabetic), and PET images were obtained 60 min later. The acquisition time was 16 min per bed position (40% TX and 60% EM). PET transmission images were segmented using a fuzzy clustering algorithm.[3] The images were scatter corrected and reconstructed using NAW-OSEM.[41] The default parameters used in clinical routine were applied (two iterations, eight subsets) followed by a postprocessing Gaussian filter (kernel FWHM=6.0 mm). The voxel size was set to $3.4\times3.4\times3.4$ mm^3.

III. RESULTS

In the subsections that follow, a basic comparison of the results obtained using the spatial domain Markov model and the wavelet domain Markov model is described. The purpose of the results in this paper is to provide evidence of the advantages achievable utilizing the multiscale methodology. To perform this, feedback from clinical scientists aids in determining PET image volumes that are not segmented effectively using spatial domain segmentation models; explicitly, three clinical data sets were selected for illustration:

- patient#1, scan 1 ($128\times128\times128$);
- patient#2, scan 1 ($128\times128\times80$); and
- patient#2, scan 2 ($128\times128\times80$). This is the same patient as above scanned several weeks after the first scan following chemotherapy.

Some illustrations of the segmentations of these problematic image volumes using both spatial and wavelet domain models are shown in this section. Figure 8 shows a 3-D rendering of a clinical study (patient#2, second visit) and a plot of BIC against varying number of clusters K. This graph indicates that the BIC plateau begins at $K=7$, which is regarded as the optimal choice of K for this model. A six-level *à trous* wavelet decomposition is performed and the first two redundant wavelet scales along with the original image are selected to refine the marginal segmentation.

A. Phantom segmentation analysis

An illustration of the process required to segment the phantom image volume is depicted in Fig. 9. In this figure, three transaxial slices representing the original slices before segmentation, corresponding slices of the two selected wavelet scales (scales one and two), and the resulting segmented slices in six clusters, respectively, are illustrated to prove the 3-D nature of the segmentation system. The inherent features of these images are clearly defined with thresholding successfully removing problematic high metabolic uptake. Due

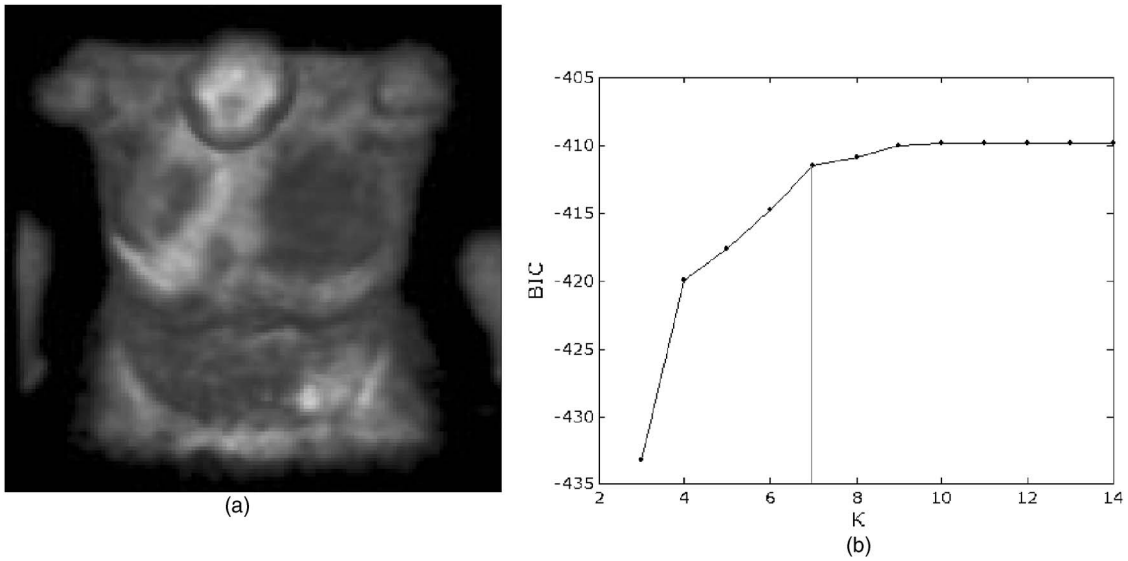

FIG. 8. (a) 3-D rendering of clinical oncology study. (b) Plot of Bayes information criterion (BIC) values for clinical patient data (scaled by a factor of 10^4). The line indicates the optimal value of the number of clusters K.

to thresholding, segment 1 representing the background has a mean close to zero and an extremely high segment probability. The quality of the segmentation provides vital information from a metabolic perspective. The obvious lesion is defined clearly and its transaxial area varies appropriately through this plane. In slice 29, segment 3 grows suitably in the right half of the slice due to a tumor insert, which becomes apparent in the succeeding slices.

Subsequently the segmented tumors resulting from application of three segmentation algorithms including the new proposed technique were measured in terms of volume by multiplying the number of voxels belonging to cluster number six ($K=6$) by the elementary voxel volume. The true lesion volumes are then compared with the actual volumes computed by the segmentation algorithms. This kind of analysis provides useful insight into the accuracy and quality of solutions provided by the algorithm. Details regarding the size and location of each tumor insert are shown in Table I. The calculated volumes and relative errors obtained using different segmentation methodologies including standard k-means, spatial domain MRFM, and the new multiscale MRFM are also depicted.

B. Clinical segmentation analysis

In the following subsections, each of Figs. 10–12 consists of six images. Each of the six images relates to one transaxial image slice of a specific 3-D image volume. Image (a) shows a transaxial image slice under normal conditions, while image (b) is a contrast enhanced version of image shown in (a). Contrast enhancement refers simply to viewing images using different window/level settings to facilitate display of lesions having abnormal uptake. Images (c) and (d) are transaxial slices taken from the first and second wavelet scales of the original 3-D image. Image (e) is a slice of the resulting 3-D segmentation of the original volumetric image using a spatial domain MRFM, and image (f) depicts a slice of the resulting 3-D segmentation map of the original image volume utilizing the wavelet domain MRFM. In each of the following examples, a logical estimate of the number of appropriate segmentation levels is used.

1. Patient#1, scan 1

Slice 34, shown in Fig. 10(a), conveys several large hypermetabolic regions; however, through manual contrast enhancement, it becomes apparent that the large hypermetabolic regions are not solely associated with tumors. Through analysis of both the contrast enhanced slice and individual wavelet scales, it is clear that five separate malignant masses are present at this transaxial location. Tumors are located on the heart/lung boundaries and on the external boundary of the right lung. When segmented into eight regions using a spatial domain model [shown in Fig. 10(e)], a reasonable result is achieved. When contrasting this result with the original image slice under normal conditions [shown in Fig. 10(a)] a solution is obtained that pinpoints the large hypermetabolic regions, though the nature of these regions remains unclear. It is difficult to determine, without manipulation, whether these hypermetabolic regions are associated with active tissues, huge cancerous masses, or a combination of both.

To perform a multiscale segmentation, redundant wavelet scales one and two are utilized. Good quality segmentation is achieved using this multiscale approach. Using the same number of clusters as the spatial domain segmentation, all the important information gained is still evident, but, in addition, the hypermetabolic regions are further divided, clarifying the position of the five tumors.

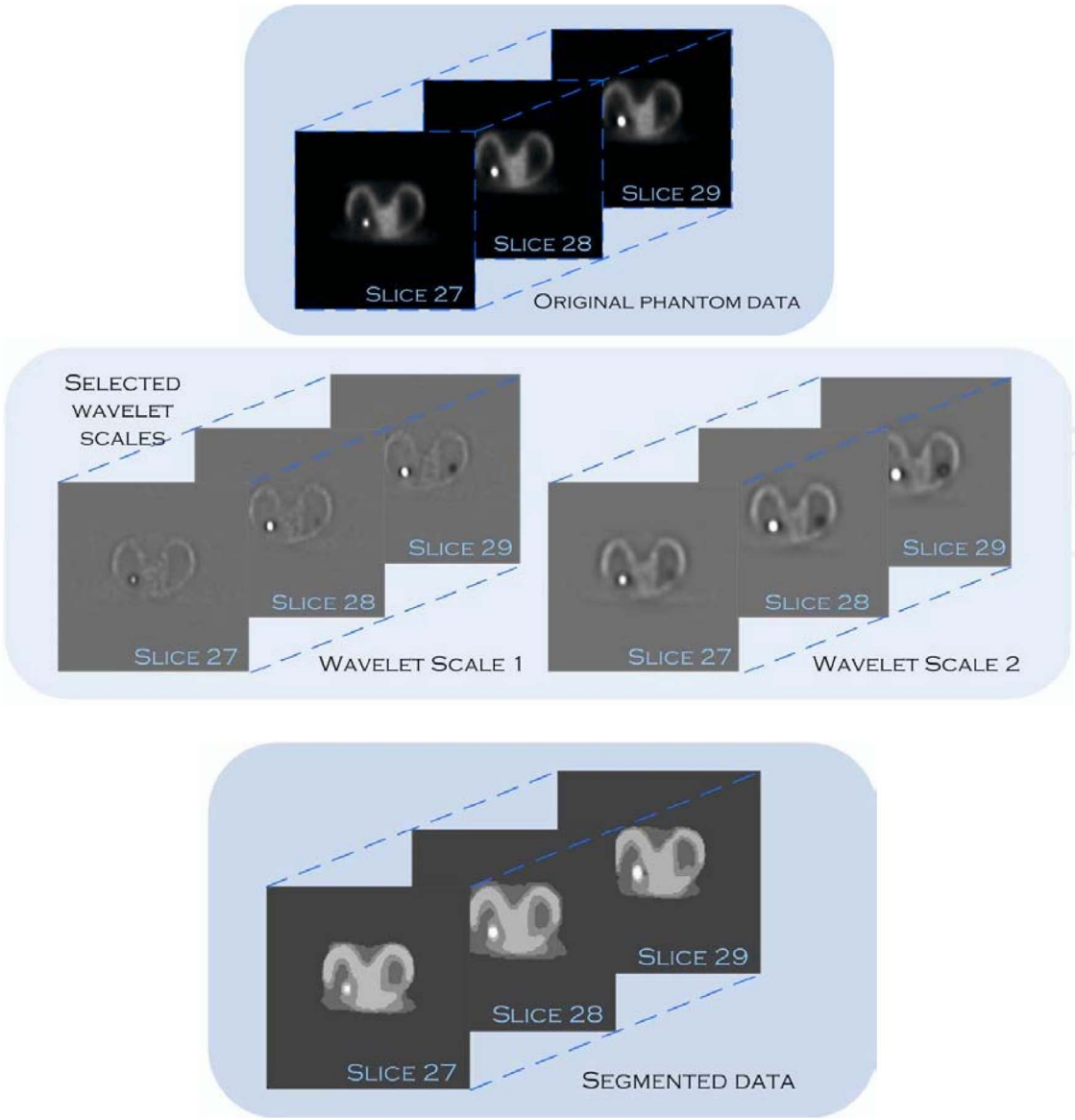

FIG. 9. Transaxial slices of anthropomorphic phantom study showing (a) original slices, (b) slices from selected wavelet scales, and (c) final segmented slices.

2. Patient#2, scans 1 and 2

The analysis of these scans has been combined to reduce repetitiveness, as both scans, although taken several months apart, are acquired from the same patient, thus revealing the same underlying oncological condition. This patient suffers from cancer at an advanced stage. Due to late diagnosis, the primary cancer has developed and spread throughout the body, producing secondary tumors also called metastases. Contrast enhancement [shown in Fig. 11(b)] of scan 1, slice 24, reveals multiple metastases in the upper regions of both

TABLE I. Comparison of tumor volumes and relative errors (%) between the true and the calculated volumes for the different segmentation algorithms assessed including *k* means, traditional MRFM, and multiscale MRFM. The relative error is defined as the difference between the calculated and the true volumes divided by the true volume. The geometry, location, and volume of tumor inserts within the experimental anthropomorphic phantom are also given.

Tumor no.	Location	True volume (ml)	*k* means (ml)	% difference	MRFM (ml)	%difference	Multiscale MRFM (ml)	% difference
1	Upper left lung	1.437	1.251	−12.93	1.574	9.54	1.332	−7.31
2	Upper right lung	1.437	1.291	−10.12	1.574	9.54	1.332	−7.31
3	Lower left lung	3.054	2.865	−6.17	3.188	4.40	2.946	−3.53
4	Lower right lung	3.054	2.865	−6.17	3.188	4.40	2.986	−2.21

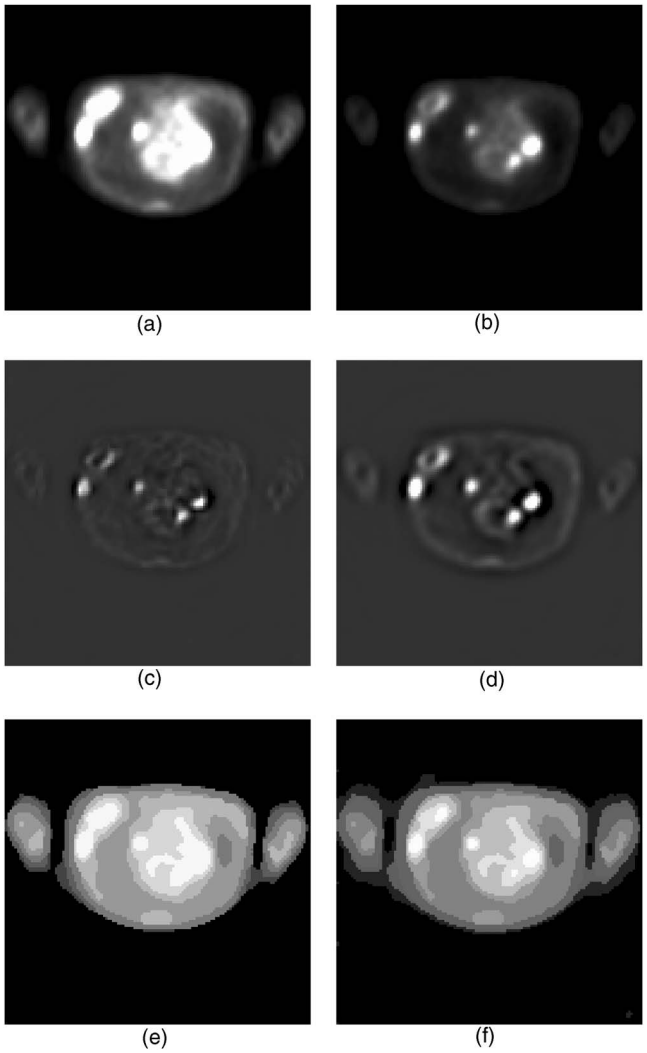

FIG. 10. (a) Original and (b) contrast enhanced version of image shown in (a). (c) Transaxial slice from the first wavelet decomposition of scan 1, patient#1. (d) Transaxial slice from the second wavelet decomposition of scan 1, patient#1. (e) Transaxial slice of resultant segmentation utilizing traditional MRFM (eight segments). (f) Transaxial slice of resultant segmentation using multiscale MRFM (eight segments).

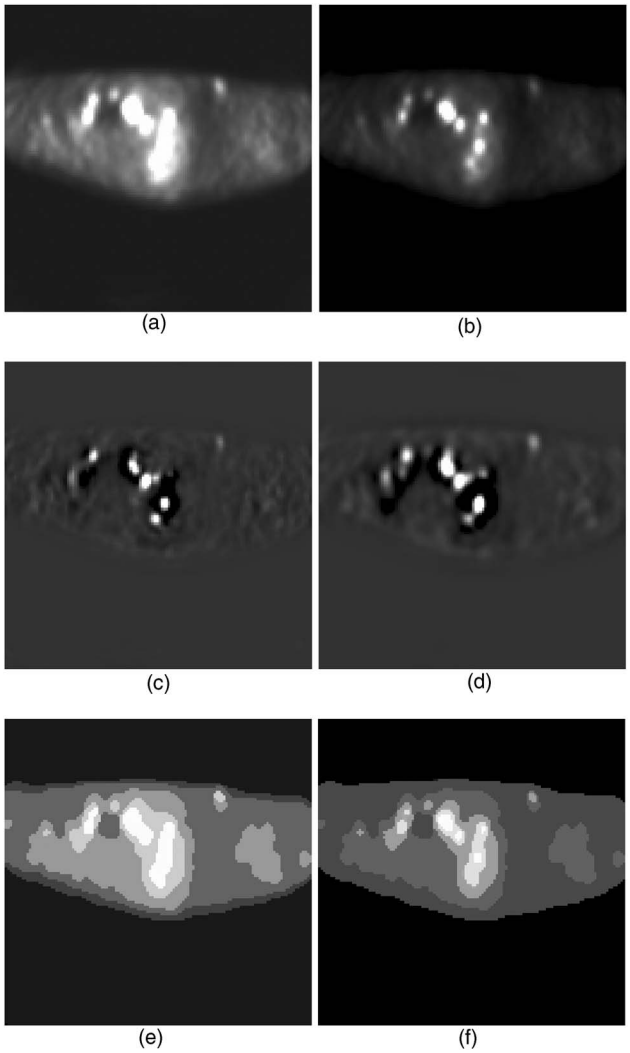

FIG. 11. (a) Original and (b) contrast enhanced version of image shown in (a). (c) Transaxial slice from the first wavelet decomposition of scan 1, patient#2. (d) Transaxial slice from the second wavelet decomposition of scan 1, patient#2. (e) Transaxial slice of resultant segmentation utilizing traditional MRFM (six segments). (f) Transaxial slice of resultant segmentation using multiscale MRFM (six segments).

lung walls. When segmented in the spatial domain in six clusters, all hypermetabolic regions are clearly defined; however, as in the previous example, the nature of these hypermetabolic regions cannot be ascertained.

For multiscale segmentation into six clusters, again, the first two wavelet scales are utilized. This segmentation [shown in Fig. 11(f)] effectively splits the hypermetabolic regions defined in the spatial domain, to pinpoint the location of several metastases. In this instance, a six-level segmentation is utilized due to the lack of variation evident in the tissue regions of the image volume, and also as a consequence of the reduced z-axis dimensionality of the image.

Figure 12(b) depicts the contrast enhanced version of scan 2, slice 33. Metastases are evident on the external walls of both lungs and in close proximity to the heart. As was found in the previous cases, spatial domain segmentation into eight clusters provides a satisfactory separation of active and non-active features. In contrast, multiscale segmentation utilizing wavelet scales one and two provides a far superior segmentation. The exact location of each individual secondary tumor is clearly visible.

IV. DISCUSSION

The role of PET during the past decade has advanced rapidly from that of a pure research tool to a methodology of immense clinical potential. FDG-PET is extensively used in the diagnosis, staging, and assessment of tumor response to therapy, since metabolic changes generally precede the more conventionally measured parameter of change in tumor size.[1] Manual and automated segmentation of patient data for the purpose of quantifying tumor size and uptake has received significant attention during the last decade. At present, segmentations are mainly performed manually by medical specialists. Although, for a typical 3-D data set, the entire expert

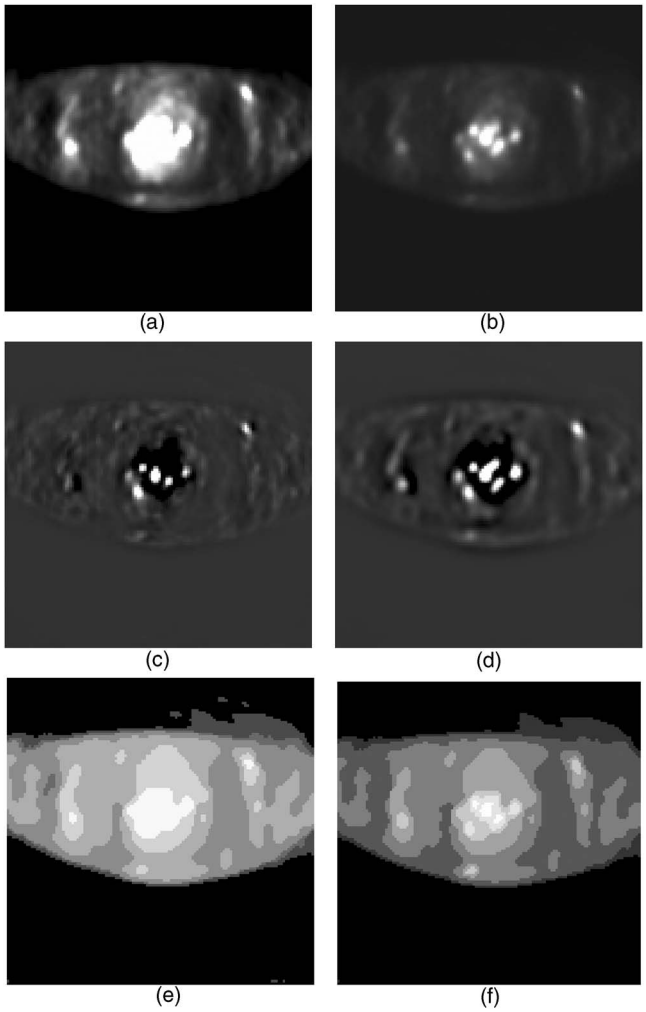

FIG. 12. (a) Original and (b) contrast enhanced version of image shown in (a). (c) Transaxial slice from the first wavelet decomposition of scan 2, patient#2. (d) Transaxial slice from the second wavelet decomposition of scan 2, patient#2. (e) Transaxial slice of resultant segmentation utilizing traditional MRFM (eight segments—only seven are visible). (f) Transaxial slice of resultant segmentation using multiscale MRFM (eight segments).

manual segmentation can take several hours to compute, this approach is perhaps the most reliable and accurate method of medical image segmentation. This is due to the immense complexity of the human visual system, a system well suited to this task. Nevertheless, the method suffers from the lack of objective assessment and reproducibility. To limit intra- and interobserver dependence and variability, the development of unsupervised segmentation algorithms is highly desired.[10]

It is apparent from Table I that the exploitation of *k*-means clustering significantly underestimates tumor volumes. This was expected as this methodology relies solely on voxel intensity and does not consider the spatial location of voxels. For the smallest lesions (~7 mm radii), the relative error is substantial (~10–13%). This large error, however, is understandable for an object of this size (relative to the spatial resolution of the PET scanner) as reallocation of one voxel at this resolution alters the relative error by 2.8%. For the larger lesions (~9 mm radii), the percentage error is much lower (~6.2%), as in this instance one voxel reallocation modifies the percentage error by only 1.3%. It is also evident that a traditional MRFM tends to overestimate tumor volume. The overestimations are at slightly reduced levels compared to the underestimations reported for the *k*-means algorithm. The substantial overestimation of volumes occurring in this case is the result of the algorithm's tendency to classify partial volume voxels as tumor cluster (cluster 6). By far the best solution for tumor quantification is the novel multiscale MRFM. This approach finds a compromise between the two aforementioned methodologies. For the smaller lesions (1 and 2), the relative error is dramatically reduced to less than 8%, whereas for the larger lesions, the relative error is less than 3.5%.

A detailed analysis of intermediate and final characteristics of each of the seven clusters for the clinical study shown in Fig. 12 showed that the mean and probability of each cluster are evident after marginal segmentation and after spatial refining. This data set is considered to be moderately problematic in terms of image contrast. Obviously, the sum of all segment probabilities is equal to one. Observation of the changes in cluster membership, which occur as a result of multiscale spatial modeling, prove that a considerable number of voxel reallocations take place, with the most significant voxel reallocations occurring in clusters 6 and 7. The number of tumor cluster 7 is reduced considerably after applying the multiscale algorithm. In addition, the mean value associated with this cluster increases significantly. The multiscale system developed efficiently divides large regions associated with high tracer uptake enabling tumors and other highly active organs or tissues to be classified separately. The characteristics of segment number 1 are completely different from the remaining segments. Both mean values associated with this segment are close to zero as a direct consequence of the thresholding procedure introduced in the algorithm. As this segment obviously represents image background, the probability of a specific voxel being a member of this segment is exceptionally high, and, in this case, there is approximately a 75% chance of a specific voxel being allocated to this class.

The developed multiscale MRFM algorithm provides a useful mechanism for identifying primary lesions and secondary metastases in image regions depicting high levels of tracer uptake. Unfortunately, this approach requires significantly more computation as the spatial domain MRFM. For an image with dimensionality $128 \times 128 \times 117$, the multiscale MRFM, initialized via MDKEM, takes approximately 30 min (C source code) to compute, for a predetermined number of clusters. Times are obtained using a single-processor 2.4 GHz Pentium 4, with 256 MB of RAM. One of the potential applications of this technique is to guide track tumor volume change to assess the response to therapy and PET/CT-based radiation therapy treatment planning by providing additional information that is important for defining the target volume, thus allowing us to alleviate the difficult time-consuming manual procedure. PET/CT plays an important role in guiding radiation treatment planning in cancers of the brain, head and neck, cervix, and other areas including lymphoma and melanoma.[8] These examples are

not exhaustive, but indicate the potentially important role of dual-modality imaging in guiding radiation treatment planning in comparison to techniques that use anatomical imaging with CT alone and the relevance of the developed methodology for this kind of applications.

V. CONCLUSION

This paper described how the traditional spatial domain MRFM, initialized by marginal segmentation, can be used to segment a 3-D image volume by characterizing the spatial relationship between neighboring voxels. In addition, this study has outlined how this model can be extended into the wavelet domain, so features evident only in certain wavelet scales can be used to refine the initial clustering solution. An anthropomorphic phantom study and selected clinical image volumes were used to portray the contrasting solutions obtained in the spatial and wavelet domains. In all cases, superior results were obtained utilizing multiple scales. This approach both determined the hypermetabolic regions observable using spatial domain modeling and the nature of these active regions by further splitting. A disadvantage of this new model is the increase in resources required to process both selected wavelet scales along with the original image volume, thus considerably increasing the complexity of the system. The algorithm is being further refined and validated in a prospective study using *in vivo* macroscopic surgical specimen of oncologic patients through qualitative and quantitative comparison of our results with the surgical specimen considered as the gold standard.

ACKNOWLEDGMENTS

This work was supported by the Swiss National Science Foundation under Grant No. SNSF 3152A0-102143. The authors gratefully thank the anonymous reviewers for useful comments on the manuscript.

[a]Author to whom correspondence should be addressed. Electronic mail: habib.zaidi@hcuge.ch

[1]D. A. Mankoff, M. Muzi, and H. Zaidi, "Quantitative analysis in nuclear oncologic imaging," in *Quantitative Analysis of Nuclear Medicine Images*., edited by H. Zaidi (Springer, New York, 2006), pp. 494–536.
[2]J. Keyes, "SUV: Standard uptake value or silly useless value?," J. Nucl. Med. **36**, 1836–1839 (1995).
[3]H. Zaidi, M. Diaz-Gomez, A. O. Boudraa, and D. O. Slosman, "Fuzzy clustering-based segmented attenuation correction in whole-body PET imaging," Phys. Med. Biol. **47**, 1143–1160 (2002).
[4]H. Zaidi, M.-L. Montandon, and D. O. Slosman, "Magnetic resonance imaging-guided attenuation and scatter corrections in three-dimensional brain positron emission tomography," Med. Phys. **30**, 937–948 (2003).
[5]A. O. Boudraa *et al.*, "Delineation and quantitation of brain lesions by fuzzy clustering in positron emission tomography," Comput. Med. Imaging Graph. **20**, 31–41 (1996).
[6]I. J. Kalet and M. M. Austin-Seymour, "The use of medical images in planning and delivery of radiation therapy," J. Am. Med. Inform Assoc. **4**, 327–339 (1997).
[7]I. F. Ciernik, M. Huser, C. Burger, J. B. Davis, and G. Szekely, "Automated functional image-guided radiation treatment planning for rectal cancer," Int. J. Radiat. Oncol., Biol., Phys. **62**, 893–900 (2005).
[8]A. C. Paulino, W. L. Thorstad, and T. Fox, "Role of fusion in radiotherapy treatment planning," Semin Nucl. Med. **33**, 238–243 (2003).
[9]E. C. Ford *et al.*, "Tumor delineation using PET in head and neck cancers: Threshold contouring and lesion volumes," Med. Phys. **33**, 4280–4288 (2006).
[10]A. Boudraa and H. Zaidi, "Image segmentation techniques in nuclear medicine imaging," in *Quantitative Analysis of Nuclear Medicine Images*, edited by H. Zaidi (Springer, New York, 2006), pp. 308–357.
[11]P. K. Sahoo, S. Soltani, and A. K. C. Wong, "A survey of thresholding techniques," Comput. Vis. Graph. Image Process. **41**, 233–260 (1988).
[12]N. Otsu, "A thresholding selection method from gray-level histograms," IEEE Trans. Syst. Man Cybern. **9**, 62–66 (1979).
[13]T. Jiang, M. B. Merickel, and E. A. Parrish,"Automated threshold detection using a pyrmaid data structure," Proc. 9th International Conference on Pattern Recognition, pp. 689–692 (1988).
[14]Y. E. Erdi *et al.*, "Segmentation of lung lesion volume by adaptive positrone mission tomography image thresholding," Cancer **80**, 2505–2509 (1997).
[15]B. Yaremko *et al.*, "Thresholding in PET images of static and moving targets," Phys. Med. Biol. **50**, 5969–5982 (2005).
[16]D. T. Long, M. A. King, and J. Sheehan, "Comparative evaluation of image segmentation methods for volume quantitation in SPECT," Med. Phys. **19**, 483–489 (1992).
[17]J. F. Daisne *et al.*, "Tri-dimensional automatic segmentation of PET volumes based on measured source-to-background ratios: influence of reconstruction algorithms," Radiother. Oncol. **69**, 247–250 (2003).
[18]H. Zaidi, "Organ volume estimation using SPECT," IEEE Trans. Nucl. Sci. **43**, 2174–2182 (1996).
[19]S. Li, *Markov Random Field Modeling in Computer Vision* (Springer-Verlag, Tokyo, 2001).
[20]K. Held *et al.*, "Markov random field segmentation of brain MR images," IEEE Trans. Med. Imaging **16**, 878–886 (1997).
[21]S. Geman and D. Geman, "Stochastic relaxation, gibbs distributions and the bayesian restoration of images," IEEE Trans. Pattern Anal. Mach. Intell. **6**, 721–741 (1984).
[22]K. Van Leemput, F. Maes, D. Vandermeulen, and P. Suetens, "Automated model-based tissue classification of MR images of the brain," IEEE Trans. Med. Imaging **18**, 897–908 (1999).
[23]M. Desco *et al.*, "Statistical segmentation of multidimensional brain datasets," SPIE Medical Imaging 2001: Image Processing, Vol. 4322; pp. 184–193.
[24]A. P. Dempster, N. M. Laird, and D. B. Rubin, "Maximum likelihood estimation from incomplete data via the EM algorithm," J. R. Stat. Soc. Ser. B (Methodol.) **39**, 1–38 (1977).
[25]P. Congdon, *Bayesian Statistical Modelling*, 2nd Edition (Wiley, West Sussex, 2007).
[26]G. McLachlan and T. Krishnan, *The EM Algorithm and Extensions* (Wiley, New York, 1997).
[27]T. Minka, Expectation-maximization as lower bound maximization, Tutorial available at http://research.microsoft.com/~minka/papers/em.html (1999). Accessed in 2006.
[28]H. Greenspan, J. Goldberger, and A. Mayer, "Probabilistic space-time video modeling via piecewise GMM," IEEE Trans. Pattern Anal. Mach. Intell. **26**, 384–396 (2004).
[29]D. Wishart, *Clustan Graphics Primer: A Guide to Cluster Analysis* (Clustan, Edinburgh, 2006).
[30]D. Stanford, "Fast automatic unsupervised image segmentation and curve detection in spatial point patterns," Ph.D. thesis, University of Washington, 1999.
[31]D. Stanford and A. Raftery, "Approximate Bayes factors for image segmentation: The pseudolikelihood information criterion (PLIC)," IEEE Trans. Pattern Anal. Mach. Intell. **24**, 1517–1520 (2002).
[32]F. Murtagh, A. Raftery, and J.-L. Starck, "Bayesian inference for multiband image segmentation via model-based cluster trees," Image Vis. Comput. **23**, 587–596 (2005).
[33]J. Besag, "On the statistical analysis of dirty pictures," J. R. Stat. Soc. Ser. B (Methodol.) **48**, 259–302 (1986).
[34]C. Collet and F. Murtagh, "Multiband segmentation based on a hierarchical Markov model," Pattern Recogn. **37**, 2337–2347 (2004).
[35]K. M. Rajpoot and N. M. Rajpoot,"Wavelet based segmentation of hyperspectral colon tissue imagery," 7th International MultiTopic Conference INMIC 2003, pp. 38–43.

[36]J.-L. Starck, F. Murtagh, and A. Bijaoui, *Image Processing and Data Analysis* (Cambridge University Press, Cambridge, 1998).
[37]A. Bijaoui, J.-L. Starck, and F. Murtagh, "Restauration des images multi-échelles par l'algorithme á trous," Trait. Signal **3**, 229–243 (1994).
[38]A. Jensen and A. la Cour-Harbo, *Ripples in Mathematics: The Discrete Wavelet Transform* (Springer-Verlag, New York, 2001).
[39]D. W. G. Montgomery, A. Amira, and F. Murtagh,"An automated volumetric segmentation system combining multiscale and statistical reasoning," Proceedings IEEE International Symposium on Circuits and Systems (ISCAS 2005), pp. 3789–3792.
[40]D. W. G. Montgomery, A. Amira, and F. Murtagh,"Automated multiscale segmentation of oncological cerebral MR image volumes," Proceedings of the IEEE International Conference on Computer Systems and Information Technology, Algiers, Algeria (2005).
[41]C. Michel *et al.*, "Preserving Poisson characteristics of PET data with weighted OSEM reconstruction," Conf. Rec. of IEEE Nuclear Science Symposium and Medical Imaging Conference, Toronto, ON, Vol. 2, pp. 1323-1329 (1998).
[42]T. G. Turkington, T. R. Degrado, and W. H. Sampson, "Small spheres for lesion detection phantoms," Nuclear Science Symposium Conference Record., 2001 IEEE, Vol. 4, pp. 2234–2237.